Materials and Design 188 (2020) 108442

Contents lists available at ScienceDirect

Materials and Design

journal homepage: www.elsevier.com/locate/matdes

Numerical analysis on coaxial one-side resistance spot welding of Al5052 and CFRP dissimilar materials

Sendong Ren [a], Yunwu Ma [a,*], Shuhei Saeki [b], Yoshiaki Iwamoto [b], Ninshu Ma [a]

[a] Joining and Welding Research Institute, Osaka University, Osaka 567-0047, Japan
[b] Dengensha Toa Co., Ltd., Kanagawa 214-8588, Japan

HIGHLIGHTS

- A coaxial one-side resistance spot welding technology was proposed to join Al5052 and CFRP sheets.
- The welding process was modeled based upon an in-house finite element code JWRIAN as a first try.
- Different from traditional RSW method, the molten zone depth in CFRP becomes larger even in cooling stage of COS-RSW process.

GRAPHICAL ABSTRACT

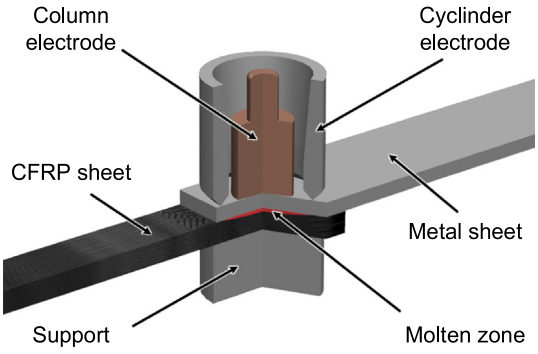

ARTICLE INFO

Article history:
Received 5 October 2019
Received in revised form 28 November 2019
Accepted 18 December 2019
Available online 24 December 2019

Keywords:
Coaxial one-side resistance spot welding
Carbon fiber reinforced plastic
Al5052
Dissimilar materials
Multiphysics coupling simulation

ABSTRACT

Carbon fiber reinforced plastic (CFRP) is a prospective lightweight material in automobile industry. However, joining metal and CFRP is a great challenge. In the present study, an innovative process called coaxial one-side resistance spot welding (COS-RSW) is proposed to fabricate Al5052 (Al) and CFRP joints. Based upon our newly developed finite element code JWRIAN, the electric-thermal-mechanical coupled process of COS-RSW is modeled and validated with experiments. The influences of welding current, welding time and electrode force on CFRP molten zone are investigated in detail. The results show that the depth of molten zone has a strong correlation with both welding current and welding time. A relative low welding current or short welding time that results in the Al/CFRP interface temperature below the melting temperature of the resin matrix is insufficient to form a sound connection between the two sheets. While excessive current or too long welding time may lead to overheating of CFRP and decomposition of the resin matrix, which increases the risk of weak joining. Furthermore, it is found that the depth of molten zone increases even at the cooling stage, which indicates accurate simulation for both the heating and the cooling stages of the COS-RSW process is indispensable.

1. Introduction

In order to reduce fuel consumption and emissions, lightweight design has been a major topic in the automotive industry. Compared with structural optimization, applying lightweight materials to substitute

* Corresponding author at: 11-1, Mihogaoka, Ibaraki, Osaka 567-0047, Japan.
E-mail address: yw.ma@jwri.osaka-u.ac.jp (Y. Ma).

https://doi.org/10.1016/j.matdes.2019.108442

traditional steels can achieve a more effective weight reduction. Aluminum alloys are increasingly used in the fabrication of lightweight vehicle bodies because of their good formability, high strength-to-weight ratio, and intrinsic recyclability. Carbon fiber reinforced plastic (CFRP) is perceived as a promising alternative for metals to cope with the ever-growing lightweight demands due to its excellent performance in strength and fatigue. Integrating aluminum alloy and CFRP in one structure offers more flexibility in lightweight product design [1,2]. Accordingly, development of reliable and economical Al and CFRP joining process is required.

To date, mechanical fastening and adhesive bonding are two common methods for combining metal and CFRP in the automotive industry [3,4]. However, they have distinct disadvantages in specific applications. Fasteners usually result in the cutting of fibers and the introduction of stress concentration, which are detrimental to the structural integrity. Adhesive bonding requires specific clamping devices and additional curing process, and the joining strength is sensitive to environmental factors. In contrast, thermal joining can avoid the above problems. In thermal joining process, CFRP is heated directly or indirectly to the melting temperature of the resin matrix. Then, the molten plastic wets the metal surface to form chemical bonds. The metals are usually subjected to mechanical or chemical surface pre-treatments to increase the bonding strength. Based on this principle, some different technologies are developed to weld plastic and metal, including laser welding, ultrasonic welding, friction welding, as well as electrical resistance welding.

Katayama and Kawahito [5] combined Type 304 stainless steel and polyethylene terephthalate (PET) by rapid laser direct joining process. The laser beam was irradiated on the PET side, passed through the transparent PET sheet and heated on the steel surface directly. They believed that the metal and plastic were tightly bonded on the atomic or molecular level, which contributed to the secure connection. Jiao et al. [6] investigated the laser joining between CFRP and 304 stainless steel by both experiment and simulation. The metal plate was heated by laser beam and the thermal conduction led to a molten zone in CFRP. The shear strength reached about 17.5 MPa. The layered structure in CFRP was considered in the numerical model and the simulated temperature distribution agreed well with the experimental results. Tan et al. [7] reported the damage characteristics of CFRP during laser joining of steel and CFRP. They observed ablation and large cavities in the center of the joint, which were surrounded by a number of porosities in the peripheral region. Liu et al. [8] studied the friction lap welding (FLW) process between AA6061 and MC Nylon-6. They reported that an increased heat input was beneficial to the joining strength due to a decline of bubbles volume at the interface. The nominal shear strength varied from 5 to 8 MPa with different welding parameters. Similarly, Amancio-Filho et al. [9] proposed that the friction spot joining (FSpJ) was able to join magnesium AZ31 with thermoplastic composites. The microstructure and hardness distribution of FSpJ joint were clarified. Although the dynamic recrystallization in stir zone directly influenced the local strength, such phenomenon was still under investigation. Goushegir [10] researched the FSpJ process between AA2024-T3 and carbon-fiber-reinforced poly (phenylene sulfide) (CF-PPS) sheets. Macro- and micromechanical interlocking, as well as adhesion force were proposed as the three primary bonding mechanisms at the interface. In addition, Balle et al. [11] investigated the ultrasonic spot welding between Al99.5 and CF-PA66. This technology formed a square weld zone and the maximum tensile strength reached 25 MPa. Monochromatic and polychromatic radiation were also employed to join thermoplastic and metal [12]. The polychromatic radiation of an infrared emitter could reduce the residual stress in joint by creating a homogeneous temperature field. Results indicates that artificial surface textures on the aluminum sheet can improve the joint strength. The largest shear strength was about 19.7 MPa. Ageorges and Ye [13] proposed a resistance welding technique to combine Al7075-T6 with CF-PEI. It was found that an additional heating element was necessary to bring the whole assembly to a high enough temperature. Insufficient or excessive energy input was detrimental to the tensile shear strength.

Resistance spot welding (RSW) is a common technology in the automotive industry, which has been employed to join metal sheets since 1920s. RSW possesses several advantages, such as short cycle time, low cost, and easy for automation [14]. However, traditional RSW process can hardly be applied to weld plastic and metal since current cannot go through the insulated plastic to form a closed circuit. To address this issue, some novel RSW processes were developed. Nagatsuka et al. [15] used an series-RSW process to join SUS304 and CFRP. Two column electrodes were located on the SUS304 side and the Joule heat was thereby generated in the steel sheet. Then, due to the heat transfer between both sheets, the resin matrix of the CFRP material was melted and the chemical bonding between the two sheets was realized. Recently, Szallies et al. [16] introduced their study about single-side resistance spot joining of polymer and metal. A pair of coaxially arranged electrodes was applied to generate a circle weld zone, the depth of which increased as a result of the increasing welding current.

According to the previous researches, welding parameters have a significant effect on the strength of plastic and metal joints. To optimize the welding parameters, a large number of experiments are usually performed, which are costly in terms of time and raw materials. Numerical simulation approach has been confirmed as an effective method for process optimization of traditional RSW process. Ma and Murakawa [17] modeled the RSW process for three pieces of high strength steel sheets based on a JWRIAN code. The minimum welding current cycles for nugget formation and weld lobe were predicted numerically. Shen et al. [18] established a two-dimensional axis-symmetric model of RSW process using an ANSYS code. The influence of stacking sequence of steel sheets on nugget size and penetration depth was discussed. Wan et al. [19] considered an improved contact interaction in RSW model of Al/zinc-coated steel joint. They proposed that the weld strength was determined by the Al nugget size and intermetallic compound thickness. However, to the best of the authors' knowledge there is few research on the numerical simulation of plastic-metal joining technology, especially the novel single-side RSW process.

In the current study, a coaxial one-side resistance spot welding (COS-RSW) technology was developed to join Al5052 and CFRP sheets. An in-house finite element (FE) code JWRIAN was updated to simulate the multi-physics coupled COS-RSW process as a first try. In the following sections, the COS-RSW experiments and tests to obtain the CFRP material properties were presented firstly, followed by the descriptions of numerical modeling details. Then the simulated molten zone profiles under different welding conditions were validated with experiments. Based on this numerical model, the temperature evolution and distribution characteristics, as well as the formation mechanism of the molten zone during COS-RSW process were revealed. The method and results

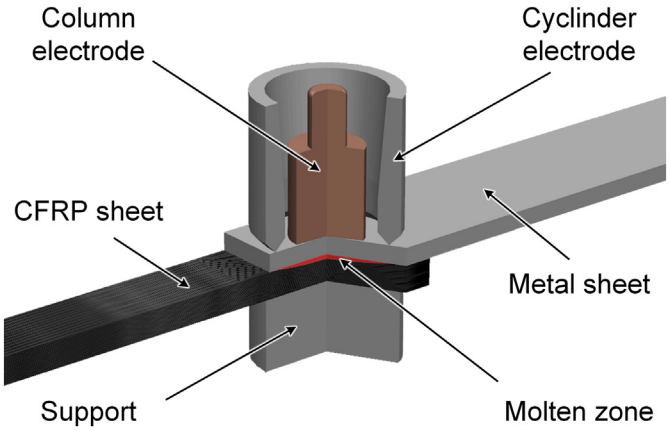

Fig. 1. Schematic of the coaxial one-side resistance spot welding process.

Table 1
Welding parameters of experiments and simulations.

Case	Welding current (A)	Welding time (s)	Electrodes force (N)
A1	2000	0.45	2450
A2	3000	0.45	2450
A3	3500	0.45	2450
A4	4000	0.45	2450
B1	3500	0.1	2450
B2	3500	0.2	2450
B3	3500	0.3	2450
B4	3500	0.4	2450
B5	3500	0.5	2450
C1	3500	0.45	1470
C2	3500	0.45	1960
C3	3500	0.45	2940
C4	3500	0.45	3430

in this study provide a reference to understand the COS-RSW process and a valuable tool to conduct process optimization.

2. Coaxial one-side resistance spot welding (COS-RSW) process

Fig. 1 depicts the schematic of COS-RSW process, which is unique in two coaxial electrodes locating on the metal side. During the welding process, the current is applied to the cylinder electrode to form a closed circuit between the electrodes and the metal sheet. Joule heat is thereby generated in the metal sheet and contact zone. The resin matrix of CFRP close to the CFRP/metal interface is liquified by thermal conduction to form a molten zone with half-lens shape. Then the molten resin wets the metal surface and chemical bonds between the two sheets are formed. In order to get a more homogeneous temperature distribution at the interface, the two electrodes were designed with different materials, i.e., CuCr for the column electrode and SUS304 for the cylinder electrode. The electrodes are fixed on copper shanks, which are contacted with cooling water at the other end. The sheets are also placed on a copper support.

3. Experimental details

3.1. Welding process

The metal sheet used in this research is Al5052 with a dimension of $75mm \times 15mm \times 2mm$. The surface of the aluminum sheet is cleaned and pretreated with silane coupling agent before welding. The CFRP is composed of 80% PA6 and 20% carbon fibers (CFs), and cut into $75mm \times 15mm \times 3mm$ sheets. The short-cut CFs are distributed in the resin matrix uniformly with random spatial orientations. Therefore, the CFRP is considered as an isotropic material in this work.

During the COS-RSW process, the two sheets are clamped with a 15 *mm* overlap. A total electrode force (F) is divided into two different parts and applied to the CuCr and SUS304 electrodes, respectively:

$$F_{CuCr} = \frac{1}{3}F$$
$$F_{SUS304} = \frac{2}{3}F \quad (1)$$

As listed in Table 1, two sets of experiments (Case A and Case B) are carried out to analyze the influence of welding current and time on the molten zone. The effect of electrodes force is discussed numerically by Case C. The holding time is fixed at 10 s in all the experiments. The specimens of Case A and B are shown in Fig. 2(a) and (b), respectively. After welding, the samples are cut along the centerline of the weld, polished following standard procedures and observed with a 3-D digital microscope (Keyence VR-3200).

3.2. CFRP properties test

Accurate temperature-dependent material properties are essential to reliable results in numerical simulation, while the properties of CFRP are sensitive to the specific components. Fig. 3 shows the measured temperature dependent thermal conductivity and specific heat of CFRP (80%PA6 + 20%CFs). The measurements are performed by JFE Techno-Research Corporation. The density of CFRP is 1.225 g/cm^3.

Meanwhile, three sets of tensile tests are carried out at different temperatures (20 °C, 100 °C and 200 °C) to clarify the mechanical properties of CFRP. The tensile specimens were fabricated according to the JIS K 7139:2009 standard (size A2), as shown in Fig. 4(a). Video extensometer was employed to accurately measure the stress-strain curves. In all the three tests, fracture appeared near to the grip sections, as shown in Fig. 4(b). The results of tensile test are given in Fig. 5. As a typical composite material, the CFRP does not show obvious yield phenomenon in the stress-strain curves. According to the BS EN ISO 527-1:1996 standard, the elastic range of plastics can be defined as the strain range from 0.05% to 0.25%. Therefore, the fitted slope within this range is deemed as the Young's modulus, and the stress value at 0.25% strain is assumed to be the yield strength, as summarized in Table 2.

Melting temperature and decomposition temperature are two critical parameters for evaluating the behaviour of plastics. The differential thermal analysis (DTA) and thermogravimetry (TG) are employed to obtain their accurate values, as shown in Fig. 6. The melting temperature is determined as the first endothermic peak in DTA curve, which is about 220 °C. The onset decomposition temperature is determined by a 5% mass fraction loss in TG curve [20], which is about 340 °C.

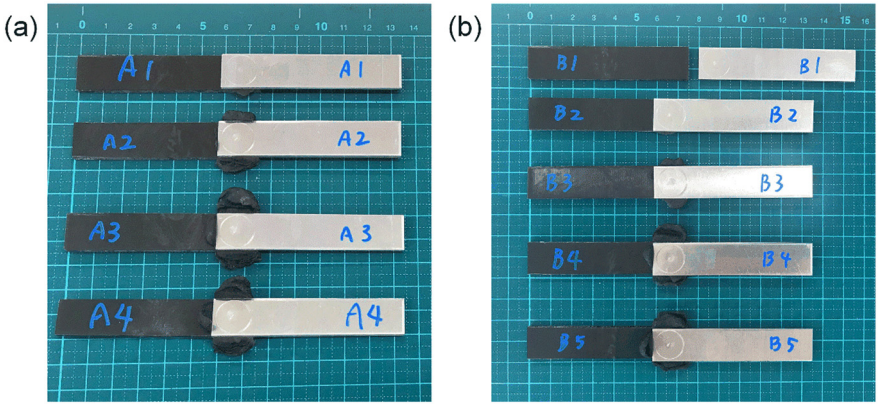

Fig. 2. COS-RSW specimens of (a) Case A and (b) Case B.

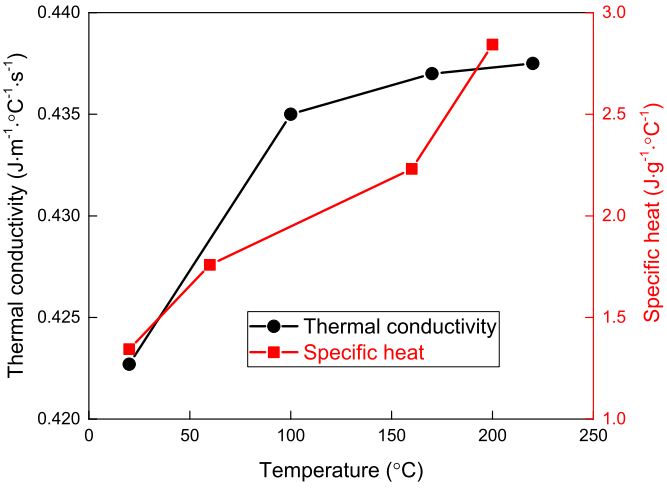

Fig. 3. Temperature-dependent thermal properties of CFRP.

4. Numerical analysis

4.1. Electric-thermal-mechanical coupled FE model

COS-RSW is a multiphysics coupled process. In current work, the electric-thermal-mechanical coupled model is described based upon the in-house FE simulation code JWRIAN [17].

In cylindrical polar coordinates, a static electrical field can be expressed by Laplace's equation:

$$\mu\frac{1}{r}\frac{\partial}{\partial r}\left(r\frac{\partial\phi}{\partial r}\right)+\mu\frac{\partial}{\partial z}\left(\frac{\partial\phi}{\partial z}\right)=0 \tag{2}$$

where μ is the electrical potential conductivity of material, which equals to the reciprocal of electrical resistivity R $[\Omega\cdot mm]$.

The electrical potential $\{\phi\}$ at structural node is solved according to the following equation:

$$[E]\{\phi\}=\{\bar{I}\} \tag{3}$$

where $[E]$ is the global electric matrix; $\{\bar{I}\}$ is the equivalent nodal current vector.

Then the current density i $[A/mm^2]$ in r and z directions as well as Joule heat generation rate per unit volume q_V $[J/(mm^3\cdot s)]$ can be calculated:

$$i_r=-\mu\frac{\partial\phi}{\partial r},\ i_z=-\mu\frac{\partial\phi}{\partial z} \tag{4}$$

$$q_V=\frac{1}{\mu}\left(i_r^2+i_z^2\right) \tag{5}$$

The governing equation for transient heat transfer analysis is given as follows:

$$c\rho\frac{\partial T}{\partial t}=\lambda\frac{1}{r}\frac{\partial}{\partial r}\left(r\frac{\partial T}{\partial r}\right)+\lambda\frac{\partial}{\partial z}\left(\frac{\partial T}{\partial z}\right)+q_V \tag{6}$$

where c, ρ and λ are specific heat capacity $[J/(g\cdot{}^\circ C)]$, density $[g/mm^3]$ and thermal conductivity $[J/(mm\cdot{}^\circ C\cdot s)]$ of materials, respectively,

The transient temperature $\{T\}$ and its rate $\{\partial T/\partial t\}$ are given as:

$$[S]\left\{\frac{\partial T}{\partial t}\right\}+[C]\{T\}=\{Q\} \tag{7}$$

where $[S]$ is specific heat capacity matrix; $[C]$ is thermal conductivity matrix; $\{Q\}$ is equivalent nodal heat.

When the transient temperature rate $\partial T/\partial t$ is expressed according to the Crank-Nicolson method, as shown in Eq. (8), the temperature $\{T\}$ after an incremental step dt can be calculated by Eq. (9).

$$\left\{\frac{\partial T}{\partial t}\right\}=\frac{\{T\}_{t+dt}-\{T\}_t}{2dt} \tag{8}$$

$$\left(\frac{1}{2}[C]+\frac{[S]}{\Delta t}\right)\{T\}_{t+dt}=\frac{1}{2}\left(\{Q\}_{t+dt}+\{Q\}_t\right)+\left(\frac{[S]}{\Delta t}-\frac{1}{2}[C]\right)\{T\}_t \tag{9}$$

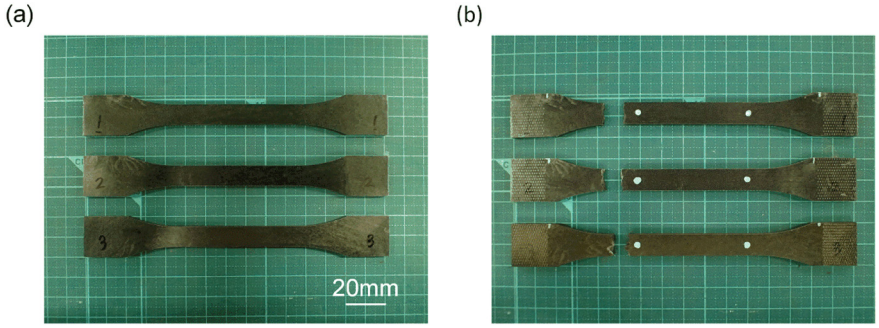

Fig. 4. (a) Tensile test specimens and (b) the fractured specimens after tensile test with the white dots showing the measuring locations by video extensometer.

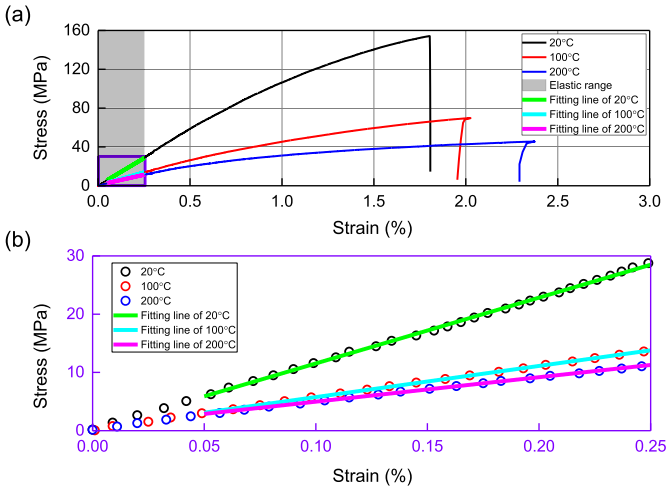

Fig. 5. (a) Stress-strain curves of CFRP and (b) zoom image of elastic region.

Table 2
Temperature-dependent mechanical properties of CFRP.

Temperature [°C]	Young's modulus [GPa]	Yield strength [Mpa]
20	11.296	28.486
100	5.349	13.789
200	4.201	11.28

The temperature filed solution is followed by mechanical analysis. The mechanical field is described using elastic-plastic FEM equation:

$$[K]\{\Delta u\} = \{\Delta F\} + \{R\} \tag{10}$$

where $[K]$ is the stiffness matrix; $\{\Delta u\}$, $\{\Delta F\}$ and $\{R\}$ represent the vector of nodal displacement, vector of nodal force as well as vector of nodal residual force, respectively.

The internal nodal displacement can lead to a strain variation $\{\Delta\varepsilon\}$, which is composed of three parts:

$$\{\Delta\varepsilon\} = [A]\{\Delta u\} \tag{11}$$

$$\{\Delta\varepsilon\} = \{\Delta\varepsilon^e\} + \{\Delta\varepsilon^p\} + \{\Delta\varepsilon^T\} \tag{12}$$

$$\{\Delta\varepsilon^p\} = \lambda\left\{\frac{\partial f}{\partial\sigma}\right\} \tag{13}$$

$$\{\Delta\varepsilon^T\} = \{\alpha\}\Delta T \tag{14}$$

where $\{\Delta\varepsilon^e\}$ is the increment of elastic strain, $\{\Delta\varepsilon^p\}$ is the increment of plastic strain, $\{\Delta\varepsilon^T\}$ is the increment strain induced by thermal expansion. f is the plastic potential and λ is a positive value of scalar. α means the instantaneous coefficient of linear expansion.

Then the stress $\{\sigma\}$ is computed according to the thermal-elastic-plastic theory:

$$\{\sigma\}_{t+dt} = \{\sigma\}_t + \{\Delta\sigma\} \tag{15}$$

$$\{\Delta\sigma\} = [D^e](\{\Delta\varepsilon\} - \{\Delta\varepsilon^T\} - \{\Delta\varepsilon^P\}) \tag{16}$$

where $[D^e]$ is the elastic matrix, $\{\Delta\sigma\}$ is the stress increment.

4.2. Dynamic contact state

COS-RSW process is accompanied by heating and softening of the sheet materials. The contact area at the electrode/Al interface keeps changing under the action of constant electrode force. Since the contact

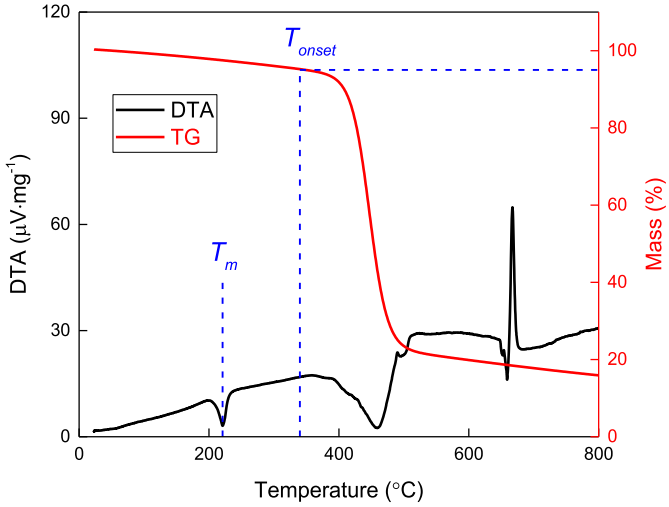

Fig. 6. DTA and TG data of CFRP.

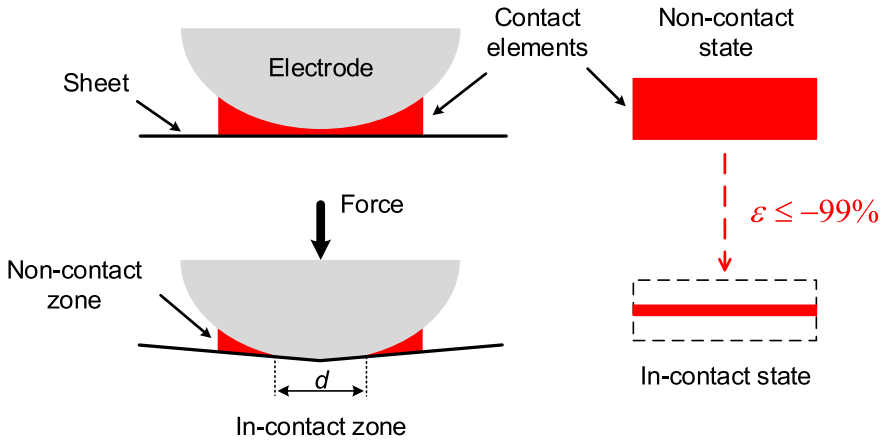

Fig. 7. Schematic of contact element and its state change criteria.

region has significant influence on Joule heat generation and thermal transfer, it is necessary to judge the instantaneous contact state in simulation.

In this study, contact elements are employed to model the change of contact state between different parts. As shown in Fig. 7, in the non-contact state, the Young's modulus, yield strength, electrical conductivity and thermal conductivity of the contact element are set to zero, i.e., the elements are treated as insulators of heat flux and current, and Joule heat is not generated. Once the strain (ε) of a contact element is lower than a threshold, the state changes to in-contact. Ideally, when

Table 3
Temperature-dependent material properties of Al5052.

T [°C]	λ	*c*	ρ	*E*	*YS*	α	*v*	*R*
24	0.15	0.9	2.68	70.3	90	2.21E-05	0.33	4.99E-05
149	0.162	1.0	2.68	62.5	90	2.38E-05	0.33	6.52E-05
260	0.2	1.125	2.68	49.5	52	2.48E-05	0.33	7.88E-05
371	0.22	1.2	2.68	35.75	21	2.57E-05	0.33	9.24E-05
580	0.254	1.25	2.68	20	3	2.64E-05	0.33	1.18E-04

Table 4
Temperature-dependent material properties of CuCr.

T [°C]	λ	*c*	ρ	*E*	*YS*	α	*v*	*R*
20	0.326	0.385	8.89	130	130	1.76E-05	0.3	2.2E-05
200	0.345	0.406	8.89	105	195	1.66E-05	0.3	3.8E-05
400	0.348	0.422	8.89	100	85	1.83E-05	0.3	4.9E-05
600	0.347	0.438	8.89	80	10	2.0E-05	0.3	6.5E-05
800	0.349	0.460	8.89	70	5	2.16E-05	0.3	8.2E-05

Table 5
Temperature-dependent material properties of SUS304.

T [°C]	λ	*c*	ρ	*E*	*YS*	α	*v*	*R*
20	0.0144	0.46	7.9	197.8	274	1.69E-05	0.29	7.13E-04
200	0.0176	0.51	7.9	184.1	199	1.79E0-5	0.29	8.02E-04
400	0.0201	0.54	7.9	167.6	157	1.90E-05	0.29	9.02E-04
600	0.0237	0.58	7.9	152.5	140	2.00E-05	0.29	1.0E-03
1000	0.0309	0.65	7.9	95.7	24	2.19E-05	0.29	1.2E-03

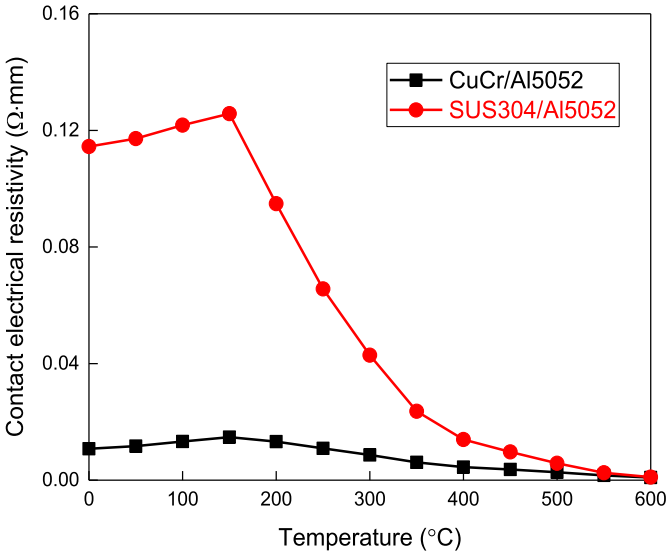

Fig. 8. Calculated contact electrical resistivity at the electrode/Al5052 interfaces.

two parts are in-contact, their distance becomes zero, corresponding to −100% strain of the contact elements. However, the −100% strain of element can cause convergence problem in numerical calculation. Therefore, in the present work, the threshold was defined as −99% to avoid convergence issue. In the in-contact state, specific values of Young's modulus, yield strength, electrical conductivity and thermal conductivity are given. In the FE model of COS-RSW process, a single-layer of contact elements is modeled, respectively, at the interfaces between electrodes/sheet, sheet/sheet and sheet/support. Therefore, the dynamic contact state between different parts can be realized numerically.

4.3. Metals properties

In addition to CFRP, the properties of Al5052, CuCr as well as SUS304 are also necessary for simulation. Since they are popular metals and have been extensively investigated, it is easy to cite the detailed data on academic papers [21–24].

The temperature-dependent material properties of metals are summarized in Tables 3–5. The thermal properties include thermal conductivity λ $[J/(mm \cdot ^\circ C \cdot s)]$, specific heat c $[J/(g \cdot ^\circ C)]$, density ρ $[g/cm^3]$. Mechanical properties include Young's modulus E $[GPa]$, yield strength, YS $[MPa]$, thermal expansion coefficient α $[1/^\circ C]$ and Poisson's ratio v. The electrical property is electrical resistivity R $[\Omega \cdot mm]$.

4.4. Contact electrical resistance

Contact electrical resistance is one of the most important components in COS-RSW, which has a significant contribution to Joule heat generation. However, this parameter is sensitive to many factors such as temperature, pressure, hardness, contamination and etc., which are difficult to quantify in experiments. Several numerical models have been proposed to describe the contact electrical resistance. Holm's formula is a well-known method, which expresses the contact electrical resistivity as a function of temperature and static contact area [25]. Moreover, Zhang et al. [26] calculated the electrical resistivity at interface according to the Wanheim and Bay's friction theory, which considered both pressure and surface conditions. In the current study, the

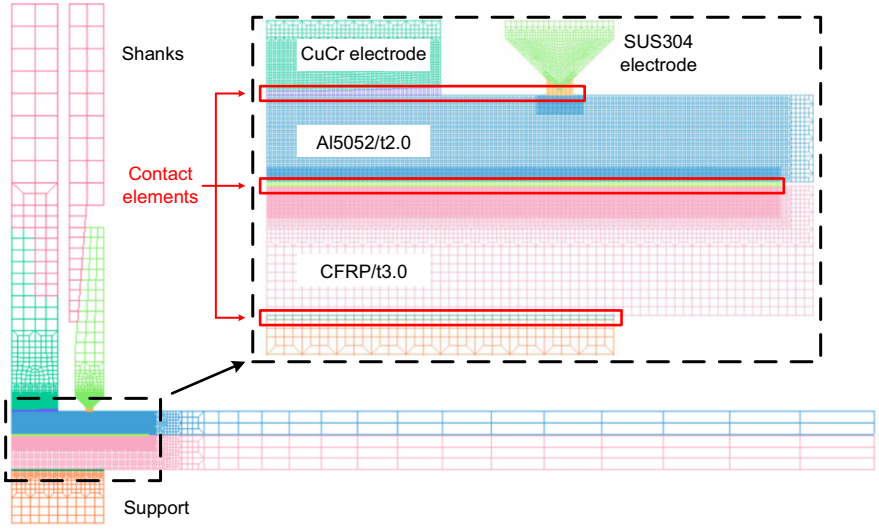

Fig. 9. Two-dimensional axisymmetric mesh.

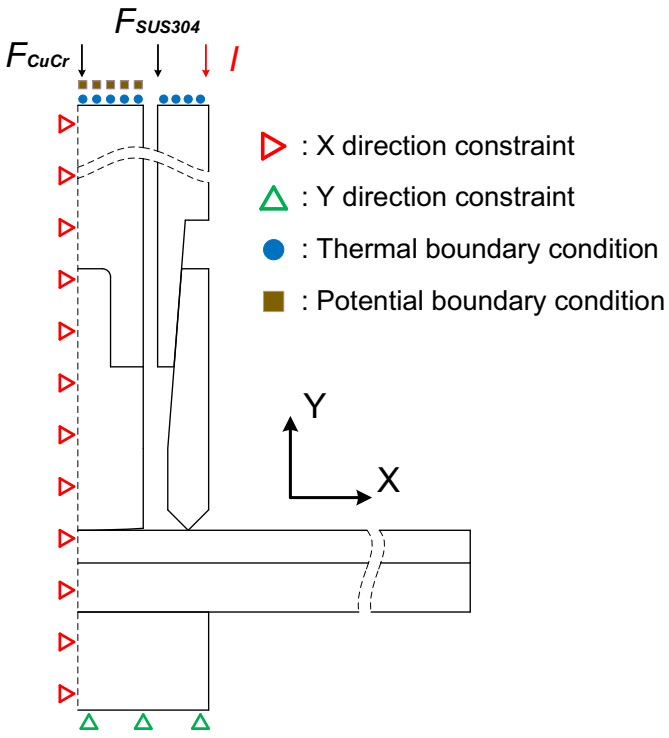

Fig. 10. Boundary conditions.

contact electrical resistivity between electrodes and Al5052 sheet is described by the following equation [27]:

$$\rho = 300 \cdot \left(\frac{\sigma_s(T)}{P}\right)^k \left(\frac{\rho_1(T)+\rho_2(T)}{2}\right) \tag{17}$$

where ρ is the contact electrical resistivity [$\Omega \cdot mm$], σ_s is the temperature-dependent yield strength of the softer metal in contact [MPa], P is pressure [MPa]. The k exponent varying from 1.0 to 1.5 is an additional factor to consider the existence of pre-treated layer on Al surface. ρ_1 and ρ_2 are electrical resistivity of the metals in contact [$\Omega \cdot mm$].The calculated contact electrical resistivities are given in Fig. 8.

4.5. FE mesh and boundary conditions

To achieve a trade-off between simulation accuracy and calculation cost, a two-dimensional axisymmetric mesh is employed in the present study, as shown in Fig. 9. According to the previous reports [28], the depth of molten region in metal-CFRP RSW joint is less than 500μm. Hence, fine enough elements with the minimum size of 25$\mu m \times 25\mu m$ are created near the interface to reflect molten zone features. The number of elements is 35,317, and that of nodes is 35,657. The total quantity of elements is reduced by transition technology.

Thermal, electrical as well as displacement boundary conditions of COS-RSW are given in Fig. 10. The initial temperature is assumed to be 20 °C. The temperature of thermal boundary is kept at 20 °C to simulate the water cooling condition in experiment. The potential at electrical

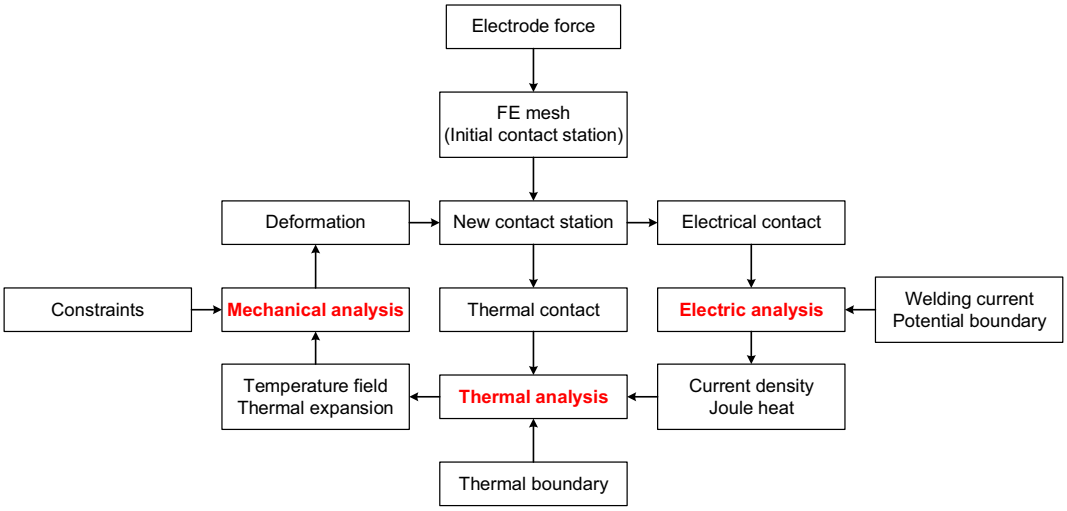

Fig. 11. Numerical analysis flowchart of COS-RSW process.

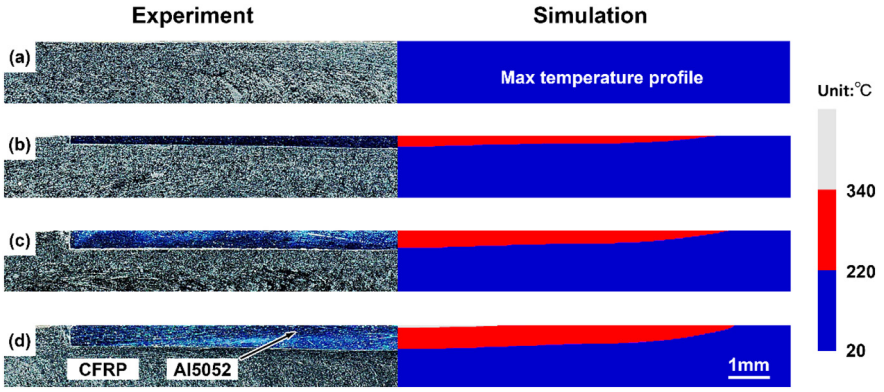

Fig. 12. Comparison of weld cross-sections and maximum temperature profiles in Case A. (a) A1: 2000A, (b) A2: 3000A, (c) A3: 3500A and (d) A4: 4000A.

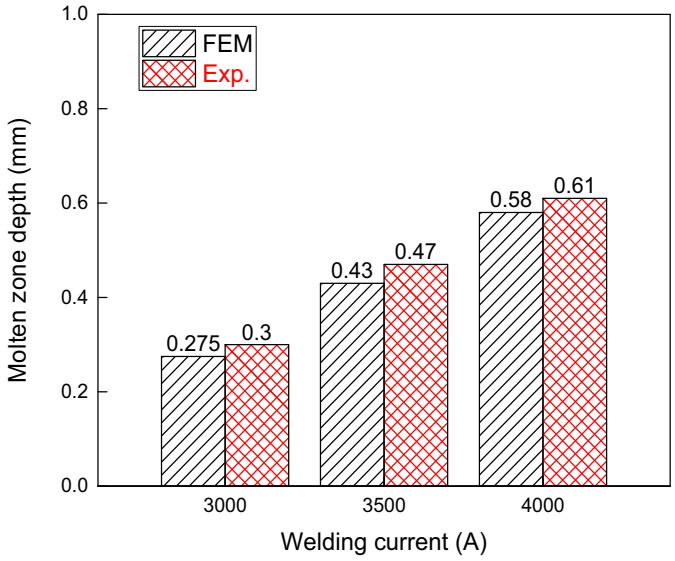

Fig. 13. Comparison of molten zone depth in Case A.

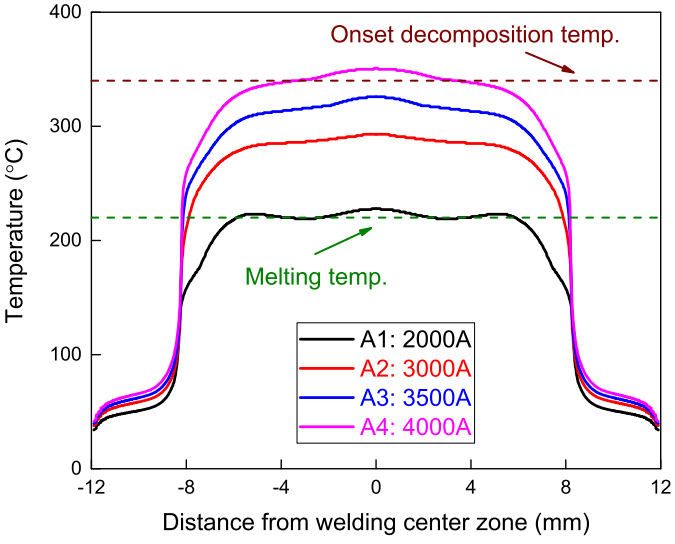

Fig. 14. Temperature distribution on the Al5052/CFRP interface in Case A.

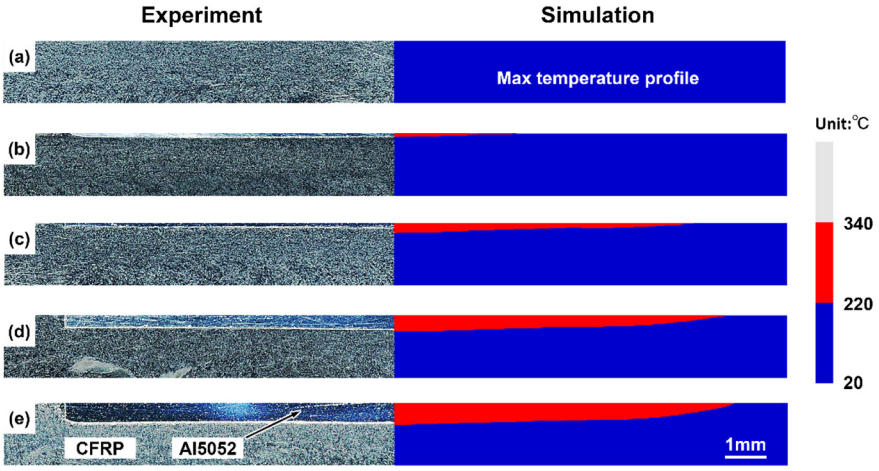

Fig. 15. Comparison of weld cross-sections and maximum temperature profiles in Case B. (a) B1: 0.1 s, (b) B2: 0.2 s, (c) B3: 0.3 s, (d) B4: 0.4 s and (e) B5: 0.5 s.

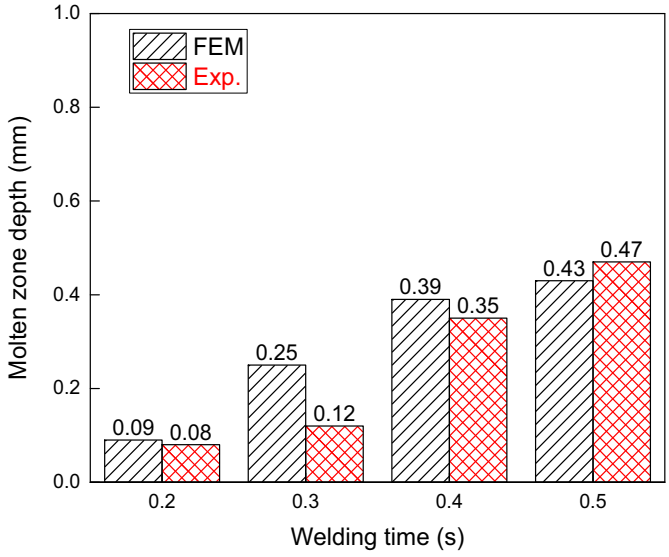

Fig. 16. Comparison of molten zone depth in Case B.

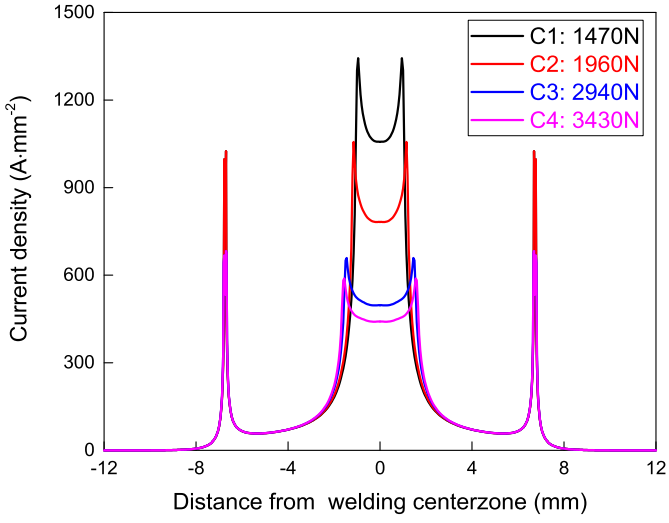

Fig. 17. Current density distribution at top surface of Al sheet in initial time.

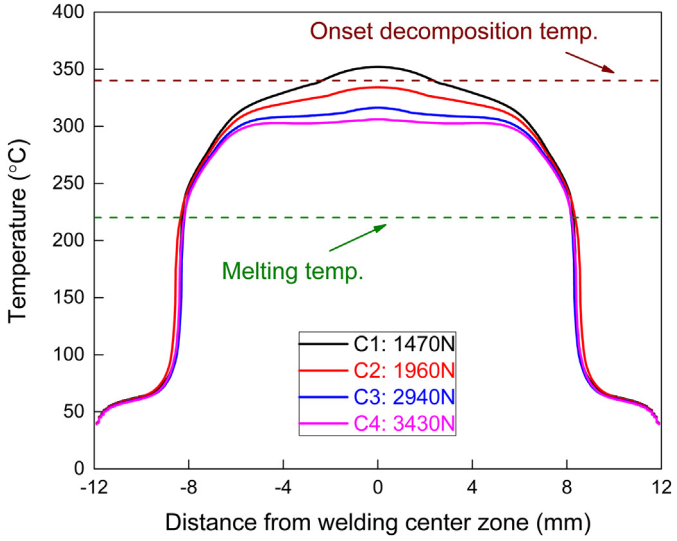

Fig. 18. Temperature distribution on the Al5052/CFRP interface in Case C.

boundary is assumed to be zero. Forces, current and displacement constraints are loaded on structural nodes.

4.6. Simulation procedure

The simulation flowchart of COS-RSW is demonstrated in Fig. 11. FE mesh depicts the initial contact conditions. Firstly, a new contact state is predicted after applying the electrode force. Then, the current density and Joule heat are calculated by electric analysis. After that, the temperature filed and thermal expansion are computed by thermal analysis. Lastly, the deformation and a new contact state are updated by mechanical analysis. This sequence is repeated in every time step until the end of calculation. The simulation of COS-RSW process covers both the welding stage and the subsequent cooling stage.

5. Result and discussion

5.1. Case A: influence of welding current

Case A aims to investigate the effect of welding current on the depth of molten zone. As shown in Fig. 2, the molten CFRP is squeezed out during welding. Hence, the Al5052 sheet is pressed into the CFRP sheet. Therefore, it is reasonable to assume that the insertion depth of Al5052 in the CFRP sheet equals to the molten zone depth in the CFRP sheet.

Fig. 12 compares the weld cross-sections with the simulated maximum temperature profiles in Case A. In the simulation results, two isothermal curves, corresponding to the melting temperature (220 °C) and the onset decomposition temperature (340 °C) of CFRP, respectively, are depicted for each case. It should be mentioned that Case A1 corresponds to a loose weld, i.e., the two sheets are still separated after welding. As shown in Fig. 12(a), there is no clear indentation in the CFRP sheet and the molten area in simulated result is also difficult to distinguish, which indicates the 2000A welding current is too small to form a sound connection. For Cases A2~A4, the profiles of melting temperatures correlate very well with the insertion depth in experiments. During the COS-RSW process, the molten CFRP is squeezed away from the overlapping area by the solid aluminum, strong interactions occur between the two materials. Therefore, a slight deformation of Al5052 sheet is observed in the cross-sections. In the simulation result of Case A4, there is a small region in the center of the weld shown gray color, which indicates the CFRP is overheated to the onset decomposition temperature of the resin matrix, refer to Fig. 12(d). This is related to the excessive welding current of Case A4.

Fig. 13 compared the molten zone depth in experiment and simulation of Case A. Obviously, the molten zone depth has positive correlation with the welding current, or the heat input. The largest value reaches about 0.6 mm. The deviation between simulation and experiment is less than 10%, which suggests that the developed numerical approach can effectively reproduce the electric-thermal-mechanical coupled process in COS-RSW.

The temperature distributions at the Al5052/CFRP interface of different welding currents are shown in Fig. 14. Although the contact electrical resistivity at the CuCr/Al5052 interface is lower than that at the SUS304/Al5052 interface, a larger contact area at the CuCr/Al5052 interface is instrumental to the heat transfer. Consequently, the highest temperature locates at the center zone of the weld. Case A1 shows a much lower interface temperature which corresponds to the lowest welding current. It is also the reason that the two sheets failed to be connected completely in Case A1. The peak temperature in Case A4 is higher than the onset decomposition temperature of the resin matrix. Overheated CFRP is risky because microbubble or ablation may appear at the interface.

5.2. Case B: influence of welding time

Unlike Case A, Case B was employed to clarify the influence of welding time on the molten zone depth. The weld cross-section and simulated maximum temperature distributions of Case B are compared in Fig. 15.

Referring to Fig. 2(b), Al5052 and CFRP sheets were not joined in Case B1. As expected, the highest temperature in corresponding simulation of Case B1 is also lower than the melting temperature of CFRP, which indicates 0.1 s is too short to form a connection. With the increase of welding time from 0.2 s to 0.5 s, molten zone appears and expands gradually in the CFRP sheet. The Al sheet starts to be pressed into the CFRP sheet at 0.2 s welding time and shows increased indentation depth with welding time.

The simulation result and measurement of molten zone depth in Case B are shown in Fig. 16. The simulated molten zone depth agrees well with experiments except for the case of 0.3 s. This discrepancy may relate to an experimental error. In general, the simulated and the measured molten zone depth have the same tendency.

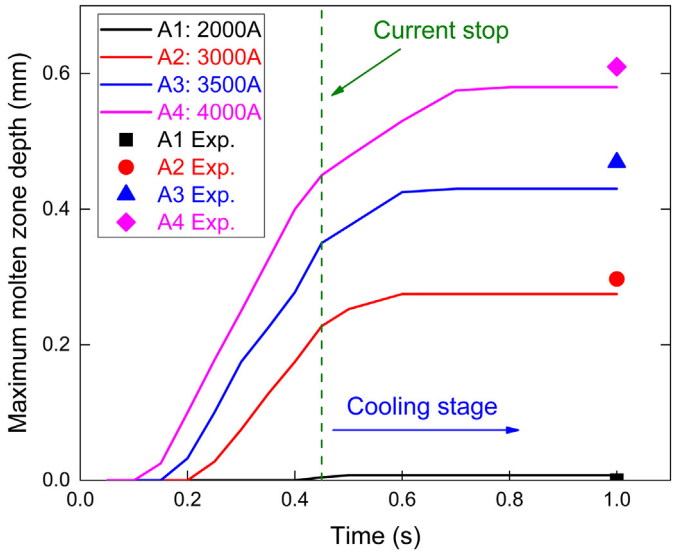

Fig. 19. The evolution of maximum molten zone depth with welding time in Case A.

5.3. Case C: influence of electrodes force

In addition to welding current and time, electrodes force is also an important factor in RSW process. Fig. 17 depicts the effect of electrodes

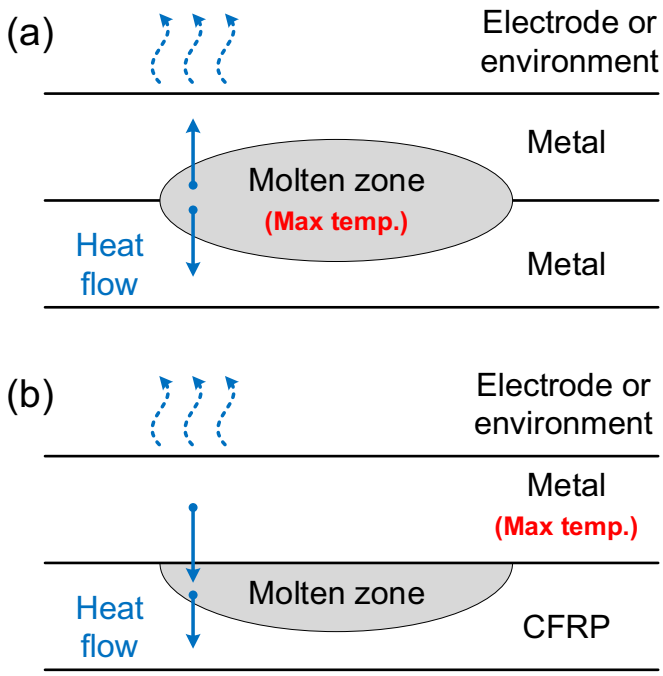

Fig. 20. Comparison of heat transfer behaviors in the cooling stage of (a) traditional RSW and (b) COS-RSW processes.

force on current density distributions on the top surface of Al sheet. Obviously, current density has a negative correlation with electrodes force. Lower force introduces smaller contact area and more significant current concentration, which is beneficial to the Joule heat generation. Since the column electrode has a sphere surface, the contact area at column electrode/Al sheet interface is more sensitive to the electrodes force compared to the cylinder electrode/Al sheet interface. Hence, with the change of electrodes force, the variation of current density is more evident in center zone.

Temperature distributions at the Al5052/CFRP interface of different electrodes force are shown in Fig. 18. In Case C1, the temperature distributes unevenly along the interface with the peak point exceeding the onset decomposition temperature of CFRP, which suggests too low electrodes force is detrimental to the welding quality. When employing a higher electrodes force, the increase of contact area decreases the unevenness of current density and establishes a better thermal transfer condition, which homogenize the temperature distribution. Generally, interface temperature shows a negative correlation with electrodes force. When the electrodes force is high enough, e.g. larger than 2940 N, the influence becomes less obvious. Therefore, it is necessary to select a sufficient electrodes force to control the Al/CFRP interface temperature within the safe range.

5.4. Evaluation of molten zone and joining strength

Fig. 19 shows the evolutions of maximum molten zone depth in Case A. Obviously, at relative high welding current, e.g. Case A4 ($I = 4000$A), the molten zone appears earlier, grows faster and ends up to a greater depth. It is interesting to notice that when it comes to the cooling stage, the welding current stops, however, the molten zone continues growing at a lower rate before reaching the final size. This phenomenon is more significant at a larger welding current.

Fig. 20 compares the heat transfer behaviors in the cooling stage of traditional RSW and COS-RSW processes. In the traditional RSW

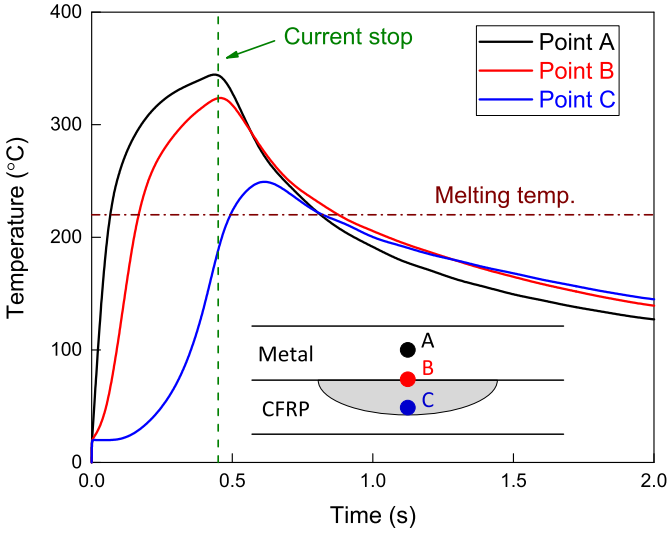

Fig. 21. The simulated temperature histories at typical locations in COS-RSW joint.

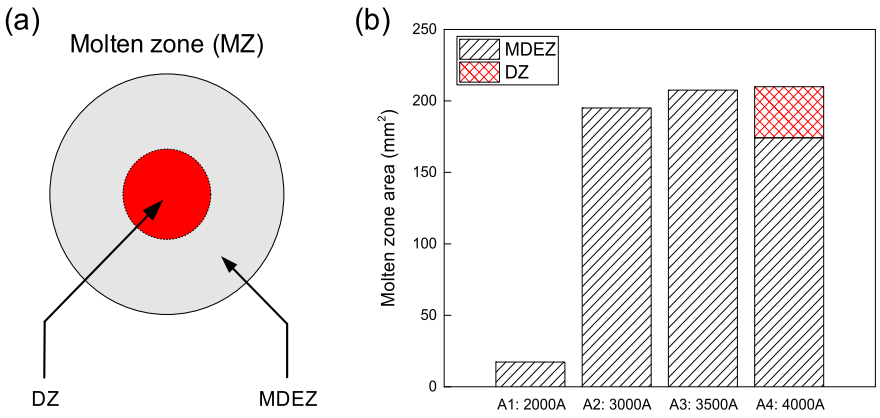

Fig. 22. (a) Division of molten zone, (b) influence of welding current on molten zone area.

process, the highest temperature appears at the center of the molten zone at the end of the welding stage, refer to Fig. 20(a). Then, in the cooling stage, the heat is transferred from the molten zone center to the surrounded metals and dissipated through the electrodes and to the environment. The nugget stops growing right after the current ceases. Therefore, in most of the numerical research of traditional RSW process, only the heating stage is considered to predict the nugget growth.

However, in the COS-RSW process, Joule heat only generates within the metal sheet and the CFRP sheet is heated by the thermal conduction from the high-temperature metal. Therefore, the highest temperature appears in the metal sheet and a large temperature gradient exists between the two sheets at the end of the welding stage. In the cooling stage, heat flow continues to go from the metal sheet to the CFRP sheet, resulting in the continued growth of the molten zone, as shown in Fig. 20(b).

The simulated temperature histories of three typical locations in Case A3 ($I = 3500$A) are given in Fig. 21. Point A locates on the metal sheet, point B is at the Al/CFRP interface, and point C is near the lower boundary of molten zone. For point A and point B, the temperature increase rapidly due to the large amount of Joule heat generation in the Al sheet. While the temperatures turn to decline as soon as the welding current stops. For point C, the temperature increases much slower during the welding stage. At the end of welding time, the temperature at point C is still lower than the melting temperature of the resin matrix. However, the temperature continues to increase and exceeds the melting temperature during the initial stage of cooling. It indicates that the molten zone in COS-RSW joint grows even in the cooling stage. Therefore, in the numerical simulation of COS-RSW process, considering the cooling stage is indispensable for the accurate prediction of the molten zone size.

In the molten zone of an COS-RSW joint, the center region possesses a higher temperature. When the temperature is higher than the decomposition temperature (DT) of the resin matrix, decomposition occurs. A melting-decomposition temperature range (MDTR) can be defined by the melting temperature and decomposition temperature, which are 220 °C and 340 °C, respectively. Therefore, the molten zone (MZ) is subdivided into a decomposition zone (DZ), where the temperature exceeds DT and a molten-decomposition evaluation zone (MDEZ), where the temperature is within MDTR. As depicted in Fig. 22(a), at the Al/CFRP interface the areas of difference zones have the following relationship:

$$A_{MZ} = A_{MDEZ} + A_{DZ} \tag{18}$$

Fig. 22(b) compares the MZ areas under different welding currents in Case A. The MZ area expands significantly with the current changing from 2000A to 3000A but increases slightly with the current from 3000A to 4000A. However, a too large welding current, e.g., 4000A, leads to the appearance of DZ and thereby reduction of MDEZ area.

In order to understand the influence of interface temperature and molten zone area on joint strength, quasi-static tensile-shear tests of the COS-RSW joints were performed. Fig. 23 presents the relationship between welding current, simulated maximum interface temperature and

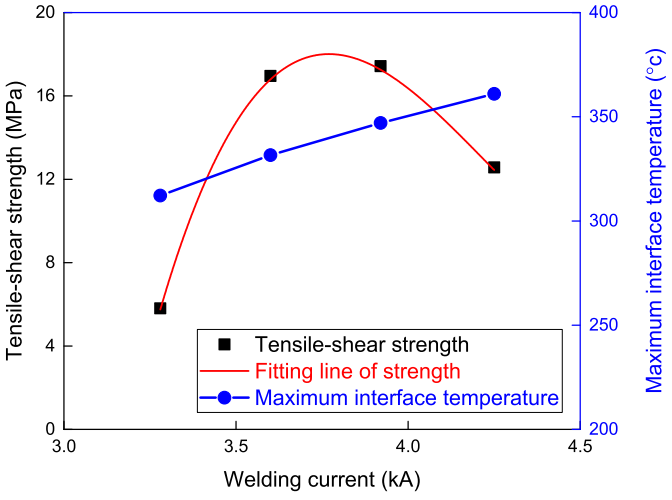

Fig. 23. Relationship between welding current, maximum interface temperature and joining strength.

tensile-shear strength. Obviously, with the increase of welding current, the maximum interface temperature increases monotonically. However, the joining strength increases firstly and then decreases, showing a similar variation tendency with that of the MDEZ area in Fig. 22(b). Decomposition of the resin matrix results in local strength loss of the CFRP sheet, which plays a negative role to the joint strength. Therefore, the area of MDEZ, which is affected by the welding time, welding current and electrodes force, can be treated as an index to evaluate the joining strength. In addition to the molten zone area, the interface temperature may also affect the chemical bonding features between the CFRP and the Al sheets. In future research, it is worthy to clarify the underlying bonding mechanism of COS-RSW joints and the effects of welding time, current and electrodes force on the joint strength.

6. Conclusions

The coaxial one-side resistance spot welding technology is developed to join Al5052 and CFRP dissimilar material sheets. A numerical approach is developed using an in-house finite element code JWRIAN to simulate the electric-thermal-mechanical coupled process of COS-RSW. The influences of welding current, welding time and electrodes force on thermal cycles, CFRP molten zone and decomposition zone are analyzed by numerical simulation and experiments. The growth mechanism of molten zone is also discussed. The following conclusions can be drawn:

(1) The simulated depth of molten zone under different welding parameters show good agreement with parallel experiments, which suggests the effectiveness of developed numerical approach.
(2) The depth of molten zone in the CFRP sheet is positively correlated with both welding current and welding time. A relative low welding current or short welding time that results in the Al/CFRP interface temperature below the melting temperature of the resin matrix is insufficient to form a sound connection between the two sheets. While excessive current or too long welding time can lead to overheating of CFRP and decomposition of the resin matrix.
(3) Electrodes force affects the distribution of current density at electrodes/Al interfaces and determines the uniformity of temperature at the Al/CFRP interface. A low electrodes force induces high concentration of current density near the two electrodes and an uneven temperature profile at the Al/CFRP interface, which is detrimental to the joining strength. Larger electrode force tends to increase the contact area, which results in a more homogeneous temperature distribution at the Al/CFRP interface.
(4) Different from traditional RSW process of metals, the depth of molten zone becomes larger even in the cooling stage of COS-RSW process. The heat transfer from high-temperature Al5052 sheet to CFRP is the driving force of continued growth of molten zone. It indicates that simulating the cooling stage is indispensable for accurate prediction of the molten zone size in COS-RSW process.
(5) Molten zone area at the Al/CFRP interface increases with welding current, however, a too large welding current leads to the appearance of decomposition zone and reduction of molten-decomposition evaluation zone. The tensile-shear strength of the COS-RSW joints shows a similar tendency with that of the molten-decomposition evaluation zone area. It is worthy to clarify the contribution of different zones on joining strength in further work.

CRediT authorship contribution statement

Sendong Ren: Conceptualization, Software, Writing - original draft. **Yunwu Ma:**Investigation, Writing - review & editing.**Shuhei Saeki:** Data curation.**Yoshiaki Iwamoto:**Resources.**Ninshu Ma:**Conceptualization, Software, Supervision.

Declaration of competing interest

None.

References

[1] J.R. Duflou, J. De Moor, I. Verpoest, W. Dewulf, Environmental impact analysis of composite use in car manufacturing, Cirp Annals-Manuf. Technol. 58 (1) (2009) 9–12.
[2] F. Rezaei, R. Yunus, N.A. Ibrahim, E.S. Mahdi, Development of short-carbon-fiber-reinforced polypropylene composite for car bonnet, Polym.-Plast. Technol. Eng. 47 (4) (2008) 351–357.
[3] J. Li, Y. Li, K. Zhang, P. Liu, P. Zou, Interface damage behaviour during interference-fit bolt installation process for CFRP/Ti alloy joining structure, Fatigue Fract. Eng. Mater. Struct. 38 (11) (2015) 1359–1371.
[4] P. Galvez, A. Quesada, M.A. Martinez, J. Abenojar, M.J.L. Boada, V. Diaz, Study of the behaviour of adhesive joints of steel with CFRP for its application in bus structures, Compos. Part B 129 (2017) 41–46.
[5] S. Katayama, Y. Kawahito, Laser direct joining of metal and plastic, Scr. Mater. 59 (12) (2008) 1247–1250.
[6] J.K. Jiao, Q. Wang, F.Y. Wang, S.P. Zan, W.W. Zhang, Numerical and experimental investigation on joining CFRTP and stainless steel using fiber lasers, J. Mater. Process. Technol. 240 (2017) 362–369.
[7] T. Xianghu, Z. Jing, S. Jiguo, S. Yang, R. Jialie, The damage characteristics and mechanism of CFRP during laser joining of CFRP/mild steel dissimilar joint, Int. Cong. Appl. Lasers Electro-Optics 2013 (1) (2013) 582–589.
[8] F.C. Liu, J. Liao, K. Nakata, Joining of metal to plastic using friction lap welding, Mater. Des. 54 (2014) 236–244.
[9] S.T. Amancio-Filho, C. Bueno, J.F. dos Santos, N. Huber, E. Hage, On the feasibility of friction spot joining in magnesium/fiber-reinforced polymer composite hybrid structures, Mater. Sci. Eng. A 528 (10—11) (2011) 3841–3848.
[10] S.M. Goushegir, Friction spot joining (FSpJ) of aluminum-CFRP hybrid structures, Weld. World 60 (6) (2016) 1073–1093.
[11] F. Balle, G. Wagner, D. Eifler, Ultrasonic spot welding of aluminum sheet/carbon fiber reinforced polymer-joints, Mater. Werkst. 38 (11) (2007) 934–938.
[12] P. Amend, S. Pfindel, M. Schmidt, Thermal joining of thermoplastic metal hybrids by means of mono- and polychromatic radiation, Laser Manufact. Lim 2013 (41) (2013) 98–105.
[13] C. Ageorges, L. Ye, Resistance welding of metal/thermoplastic composite joints, J. Thermoplast. Compos. Mater. 14 (6) (2001) 449–475.
[14] S. Aslanlar, The effect of nucleus size on mechanical properties in electrical resistance spot welding of sheets used in automotive industry, Mater. Des. 27 (2) (2006) 125–131.
[15] K. Nagatsuka, B. Xiao, L. Wu, K. Natata, S. Saeki, Y. Kitamoto, Y. Iwamoto, Dissimilar materials joining of metal/carbon fibre reinforced plastic by resistance spot welding, Weld. Int. 32 (7) (2018) 505–512.
[16] K. Szallies, M. Bielenin, K. Schricker, J.P. Bergmann, C. Neudel, Single-side resistance spot joining of polymer-metal hybrid structures, Weld. World 63 (4) (2019) 1145–1152.
[17] N. Ma, H. Murakawa, Numerical and experimental study on nugget formation in resistance spot welding for three pieces of high strength steel sheets, J. Mater. Process. Technol. 210 (14) (2010) 2045–2052.
[18] J. Shen, Y. Zhang, X. Lai, P.C. Wang, Modeling of resistance spot welding of multiple stacks of steel sheets, Mater. Des. 32 (2) (2011) 550–560.
[19] Z.X. Wan, H.P. Wang, M. Wang, B.E. Carlson, D.R. Sigler, Numerical simulation of resistance spot welding of Al to zinc-coated steel with improved representation of contact interactions, Int. J. Heat Mass Transf. 101 (2016) 749–763.
[20] D.M. Fox, J.W. Gilman, H.C. De Long, P.C. Trulove, TGA decomposition kinetics of 1-butyl-2,3-dimethylimidazolium tetrafluoroborate and the thermal effects of contaminants, J. Chem. Thermodyn. 37 (9) (2005) 900–905.
[21] D. Deng, S. Kiyoshima, FEM prediction of welding residual stresses in a SUS304 girth-welded pipe with emphasis on stress distribution near weld start/end location, Comput. Mater. Sci. 50 (2) (2010) 612–621.
[22] M.M. Hosseini, H.B. Tabrizi, N. Jalili, Thermal optimization of friction stir welding with simultaneous cooling using inverse approach, Appl. Therm. Eng. 108 (2016) 751–763.
[23] N. Jalili, H.B. Tabrizi, M.M. Hosseini, Experimental and numerical study of simultaneous cooling with CO_2 gas during friction stir welding of Al-5052, J. Mater. Process. Technol. 237 (2016) 243–253.
[24] R.A. Matula, Electrical-resistivity of copper, gold, palladium, and silver, J. Phys. Chem. Ref. Data 8 (4) (1979) 1147–1298.
[25] J. Greenwood, Constriction Resistance and the Real Area of Contact, 1966.
[26] W. Zhang, Design and Implementation of Software for Resistance Welding Process Simulations, 2003.
[27] W. Zhang, N. Bay, Finite element Modelling aided process design in resistance welding, 8th Int. Conf. on Computer Techn. in Welding, 1998.
[28] K. Nagatsuka, B. Xiao, L. Wu, K. Nakata, S. Saeki, Y. Kitamoto, Y. Iwamoto, Resistance spot welding of metal/carbon-fibre-reinforced plastics and applying silane coupling treatment, Sci. Technol. Weld. Join. 23 (3) (2018) 181–186.